Research Article | Vol. 29, No. 13 / 21 June 2021 / Optics Express 20063
Optics EXPRESS

Plasmonic gold nanojets fabricated by a femtosecond laser irradiation

YUJIA GUO,[1,4] KAIXIN ZHANG,[2,4] MING ZHANG,[1] YINGJIE CHAI,[3] YING DU,[1,5] AND GUOHANG HU[2,6]

[1]College of Science, Zhejiang University of Technology, Hangzhou 310023, China
[2]Key Laboratory of Materials for High Power Laser, Shanghai Institute of Optics and Fine Mechanics, Chinese Academy of Sciences, Shanghai 201800, China
[3]CREOL, The College of Optics and Photonics, University of Central Florida, Orlando, FL 32816, USA
[4]Y. Guo and K. Zhang contributed equally to this work
[5]duying@zjut.edu.cn
[6]huguohang@siom.ac.cn

Abstract: Gold nanojets with various morphologies, from nanopillar to nanotip with up to 800 nm height, and finally to nanotip with droplet, are fabricated on gold thin film by a femtosecond laser irradiation. The near-field localized surface plasmon resonance (LSPR) and photothermal effects of gold nanojets are studied through finite element electromagnetic (EM) analysis, supporting in nanojets design for potential applications of high-resolution imaging, nanomanipulation and sensing. For an individual nanotip, the confined electron oscillations in LSPR lead to an intense local EM field up to three orders of magnitude stronger than the incident field strength at the end of gold tip, where the vertical resolution for the field enhancement was improved down to nanoscale due to the small size of the sharp gold tip (5-nm-radius). At specific wavelength, nanopillar can serve as an effective light-to-heat converter and its heating can be fine-tuned by external irradiation, and its dimension. The long-range periodic nanojet arrays (periods from 1.5 μm to 2.5 μm) with different geometry were printed using several pulse energy levels. By confining more light into the tip (two orders of magnitude stronger than single tip), nanotip array shows more pronounced potential to serve as a refractometric sensor due to their high sensitivity and reproducibility. These results promote fs laser printing as a high-precision tool for nanoarchitecture in optical imaging, nanomanipulation and sensing application.

1. Introduction

As a nanowire, a gold nanostructure with the dimension of less than the wavelength of incident light can excite collective but non-propagating localized surface plasmon resonance (LSPR) along its apex and consequently present an extraordinary enhancement of the local electromagnetic (EM) field in the vicinity of its tip axis [1]. The local EM field enhancement on gold nanostructures can influence far-field optical signals such as fluorescence, Raman scattering and infrared absorption, which has been realized as the major contributor to the plasmon-enhanced fluorescence sensor, surface-enhanced Raman scattering and surface-enhanced infrared absorption spectroscopy for chemical detection and in vivo biological sensing application [2]. By utilizing LSPR, single nanostructure-based sensor with enhanced sensitivity to refractive index (RI) variations of analyte in close vicinity to metallic nanostructures, is capable of single-molecule detection [3–5]. Periodically patterned plasmonic nanostructures show pronounced collective LSPR [6–10], which draw more attention for different sensing applications, such as the detection of DNA sequence of molecules [11] and the specific antigen-antibody binding [12]. Moreover, the plasmonic structures offer a nanosized spot of light irradiation, which may also allow the effective applications of guiding and imaging capabilities beyond the diffraction limit, nanomanipulation and nanotrapping [13], such as optical nanoprobes [14], superlenses [15], plasmonic tweezers

#428676 https://doi.org/10.1364/OE.428676
Journal © 2021 Received 26 Apr 2021; revised 28 May 2021; accepted 3 Jun 2021; published 11 Jun 2021

Optics EXPRESS

[16]. For instance, vertically aligned nanopillars were used for in vitro single-molecule detection [17] and fluorescence imaging in live cell [18] by below-the diffraction-limit observation volume. The LSPR nanostructures, have been proven to be able to trap a single nanoparticle down to less than ten nanometers [19–24]. Also, the specific target in a multigene mixture can be precisely detected by a LSPR biosensor based on the plasmonic photothermal effect of gold nanoislands [25].

In the last few years, plasmonic nanostructures with various shapes, such as sphere [26], prism [27], triangle [28], cube [29], shell [30], rod [31], etc., have been fabricated by wet chemical methods and traditional lithography technology. However, the fabrication of structures with nanoscale tips is a challenging task using these fabrication technologies. Electrochemical etching procedures and complicated electron- and ion-beam lithography techniques have been developed to produce desired sharp edges required for LSPR purpose [32], but the reproducibility and yield of good tips are still a challenge, and make the fabrication expensive.

Since the first demonstration by Nakata in 2003 [33], femtosecond (fs) laser pulses offer a new opportunity to fabricate various sub-wavelength microstructures in metallic thin film with very high precision and reproducibility, which have become an effective nanofabrication tool in recent years [34,35]. The fabricated plasmonic nanovoids demonstrate near-field plasmon-mediated EM field enhancement, providing a tunable and spectral tuning in the mid infrared range [36]. High-throughput micropatterning of plasmonic surfaces (such as micro-hole, nanoantenna and nanovoid arrays) by fs laser pulses have been demonstrated for advanced infrared-sensing [37–40] and plasmonic coloration [41]. The nonlinear optical response from both the individual nanostructures and their ordered arrays were studied, supporting lattice-type plasmons at near-infrared wavelength [42]. Generally, most of researches investigated the geometric shape and dimensional variety of noble-metal textures versus pulse energy, and then concentrated on their reflection or scattering resonant wavelength shift with either Fourier-transform Infrared microspectroscopy [37,39,42] or confocal spectrometer [43], by fine tuning of the diameter and height of nanoviod [43], nanoantenna length and gold film thickness [36], array period [37,41], nanobump circumference length and pitch [42], pulse energy and array period [39]. However, the plasmonic structures could serve not only as a spectra-based sensor, but provide wide tasks such as optical trapping, label-free imaging, thus it is of great significant to have a better understanding of the near-field plasmonic response of various nanojets, such as their EM and photothermal field characteristics.

In this contribution we studied the EM enhancement and photothermal properties of single nanojet with three kinds of geometric features as a function of its size, incidence angle and wavelength of light, as well as the surrounding medium, which will be helpful for its high resolution imaging and optical trapping application. We also demonstrated the laser-based nanofabrication of periodic nanostructure array with high density, and analyzed the different way their resonances take place and discussed their LSPR sensing potential by comparison with single nanostructure-based sensor.

2. Materials and methods

2.1. Film preparation

A gold film with the thickness of 45 nm was coated onto a fused silica substrate using a magnetron evaporation procedure. The chamber pressure is 10^{-5} bar and the coating average speed is ~1 nm/s, while rotating the sample holder at a speed of 30 rpm to ensure the uniform deposition. The film thickness was controlled *in situ* by a microbalance system inside the vacuum chamber.

Optics EXPRESS

2.2. Femtosecond laser printing of gold nanojets

Figure 1 shows the schematic diagram of a femtosecond laser processing setup. An inverted microscope is coupled with the laser (350 fs-pulsed laser with a wavelength of 520 nm) for synchronized use. A white light is required to illuminate the sample, and the optical response image is collected through a microscope objective (Olympus, LMPLFLN 100×, NA 0.8) by a cooled charge-coupled device (CCD), which helps to find sites of interest on the surface of sample. The Gaussian beam profile of the single pulse laser was focused onto the surface of the gold thin film with the same objective. These focusing conditions yield a laser spot with a *1/e*-diameter of $1.22\lambda/\mathrm{NA} \approx 793$ nm on the thin film surface that is somewhat larger than the lateral size of the individual nanojet. The sample is placed on the 3D motion stage such that only the sample is moved while the laser focus is fixed. Depending on the applied pulse energy (14.8 nJ~23.1 nJ) which is controlled by a PC-driven attenuator, various types of nanostructures can be fabricated on the surface of gold film. A rather slow 1 kHz printing rate was used to ensure the positioning accuracy which will affect the arrangement of nanojet array.

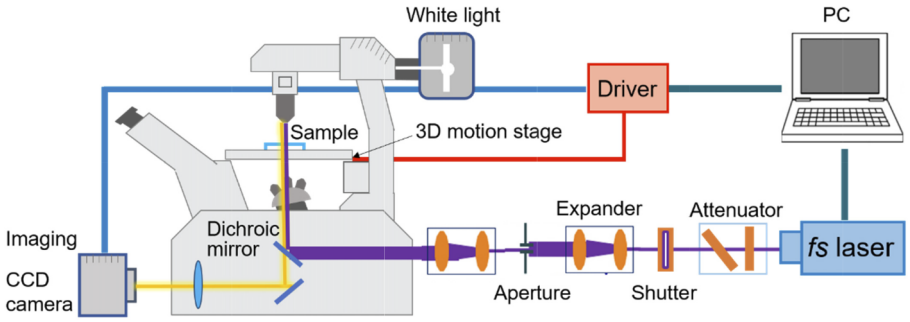

Fig. 1. Scheme for a gold nanojets fabrication setup based on fs laser system.

2.3. Measurement and characterization

The gold film thickness was verified by atomic force microscopy (AFM, Nano-Observer, CS Instruments, Villingen-Schwenningen, Germany) measurements, and the nanojets were characterized using an ULTRA 55 scanning electron microscope (SEM, Zeiss, Oberkochen, Germany) and AFM. A micro-spectrophotometer (MSV-370, Jasco, Tokyo, Japan) was used for the spectral measurements of nanotip array in an area of $300 \times 300\ \mu m^2$.

2.4. Theoretical basis of the LSPR effect and its sensing theory

For single metallic structure with feature sizes down to nanoscale, it can confine external optical field to a deep-subwavelength volume by virtue of LSPR, resulting in near-field enhancement of orders of magnitude $|E^2|$ with respect to the incident light [Fig. 2(a)]. The LSPR effect can be strongly modified by the geometry and composition of the plasmonic nanostructures, as well as the surrounding environment. The resonance condition of the LSPR is met as [44]:

$$\omega_{\mathrm{LSPR}} = \frac{\omega_p}{\sqrt{1+\kappa_1 \varepsilon_d}} \tag{1}$$

where ω_{LSPR} and ω_p are the LSPR angular frequency and bulk plasma frequency of free electron oscillation, ε_d is the permittivity of the dielectric material surrounding the nanostructure, and κ_1 is geometry factor due to the depolarization of the first order mode.

For a single isolated gold nanostructure, the LSPR effect depends on the geometrical parameters of the nanostructure, such as antenna length, circumference length, tip apex and the cone angle,

Optics EXPRESS

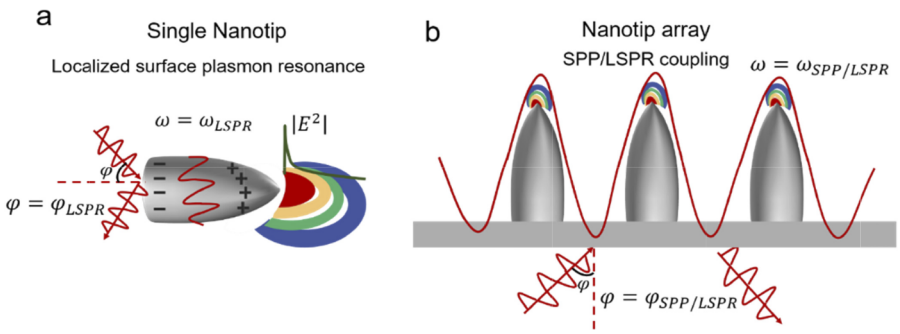

Fig. 2. (a) LSPR leads to an amplified local EM field at the end of the single nanotip. (b) LSPR/SPP coupling of nanotip array.

thin film thickness, etc. The maximum electric field position (resonant wavelength) for gold nanostructures shows almost linear dependence *versus* antenna length l [36] and circumference length L [43]. With an Au nanotip, the electric field intensity can be enhanced by two orders of magnitude, whereas the enhancement for a platinum, semiconductor or dielectric (e.g., Si or glass) nanotip, the field enhancement will drop. However, the electric field can also be much enhanced by a specially designed all-dielectric light concentrator [45]. In addition, a slight improvement of tip sharpness will lead to a significant increase of the field enhancement [46]. Besides the influences from nanotip, it is also important that LSPR conditions are strongly dependent on the angle of incidence θ, incident light wavelength λ and polarization [9].

For the assembly of gold nanostructures, the LSPR properties of individual nanostructure will be modified by the interaction with the substrate and with other nanostructure [47]. Since the gold nanojets are connected with each other by the gold thin film, the inter-nanostructure coupling is mediated by the propagating charge waves known as SPPs [48]. Since both SPP and LSPR have local fields, coupling can occur between SPP/LSPR, leading to enhanced local field and a shift in the spectral position due to hybridization between two modes, as shown in Fig. 2(b). For metallic nanostructure arrays, the collective LSPR/SPP resonances or grating effects are excited by periodic plasmonic structures with large areas, which is sensitive to the period of the nanostructures, incident angle and wavelength of light [49].

When the nanotip and illumination conditions are fixed, using the relation between the wavelength λ and the angular frequency ω, along with the conversion from ε_d to refractive index n ($\varepsilon_d = n^2$), ω_{LSPR} can be converted to the LSPR wavelength λ_{LSPR}, as:

$$\lambda_{\mathrm{LSPR}} = \lambda_P \sqrt{1 + \kappa_1 n^2} \tag{2}$$

Thus, we can find that there is a linear relationship between the LSPR wavelength and the refractive index of the surrounding medium.

2.5. Modeling and simulation

In order to calculate the EM field profiles involved the gold nanojet irradiated with an incident light, a 3D finite element method (FEM) in COMSOL software with the Wave Optics module was applied. The metal boundary condition was set at the bottom for providing a radiation boundary and the perfect matched layers approach was used at the top for providing an absorption boundary condition. The geometry considered for the nanojet surface system was based on SEM images. The tip of each nanojet is modeled by a hemisphere with a radius (r) at the end of a cone. The nanojet array model is set up for one unit cell of three jets, describing the periodicity by using periodic boundary condition. The input light is set as a Gaussian plane-wave with an incident angle φ to numerically calculate the variable-angle EM field and transmission spectra.

Optics EXPRESS

3. Results and discussion

3.1. Fabrication of sub-micrometric jets on gold film

As can be seen in Fig. 3(a), the irradiation of the gold film by the tightly focused 350 fs-pulsed laser with a wavelength of 520 nm results in the formation of submicro-sized structures. By increasing the laser energy of a single pulse, the geometrical dimensions of structures can be varied leading to its reshaping from the nanopillar, nanotip, to the nanotip with droplet. At low laser energies (14.8 nJ~17.2 nJ), nanopillar occurs with the growth of an extremely small bump. At higher laser energies (>17.2 nJ), a nanotip with sharp edge is formed with the height varying from 280 nm to 800 nm. For laser fluence equal or higher than 19.0 nJ, a droplet can occur on the top of the nanotip. However, by higher laser energy of 21 nJ, the gold nanostructuration process evolves to an unstable condition and finally results in the destruction of the nanojets. The shape, height and diameter of nanojet produced by single laser pulse with different pulse energies are concluded in Fig. 3(b), showing the growth of their dimensions-their height increases from 200 nm to 800 nm and their diameter increases slowly from 450 to 600 nm versus pulse energy. Broken arrows illustrate that starting from a 21 nJ laser pulse energy, the process becomes unstable and the nanojet structures are destroyed. The cross sections of the nanopillars at 15.4 nJ and 17.2 nJ were observed using AFM, as shown in Figs. 3(c) and 3(d), indicating that the pillar was more elongated and the top shape of pillar changed from spherical to be conical at higher laser energy. The high precision of fs laser nanostructuration allows the control of the shape, height and diameter of the nanojet as antenna structures for specific application, and also provides the possibility to produce a large-area periodic array of gold nanojet.

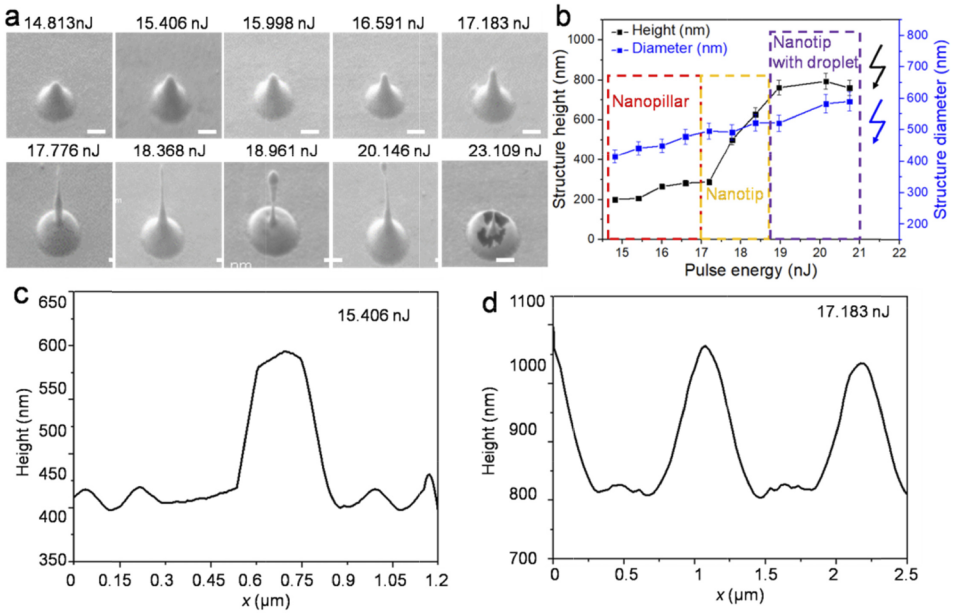

Fig. 3. (a) SEM images of nanostructures obtained by femtosecond laser radiation of 45-nm-thick Au film on glass with a single laser pulse (wavelength 520 nm, pulse duration 350 fs). The laser pulse energies are indicated in the images. Scale bar is 200 nm. (b) The height and diameter of the Au nanojets versus the laser pulse energy. Cross sections of the nanopillars (c) at 15.406 nJ and (a) at 17.183 nJ observed using AFM.

The nanojet formation by fs pulsed laser irradiation takes place due to an ablation process affected by metal flow dynamics in the molten phase due to a much slower electron–phonon

Optics EXPRESS

relaxation [50]. Figure 4 shows the formation process of various gold nanojets. When the laser pulse at below-ablation threshold fluence spatially confined onto a diffraction-limited focal spot on gold film, the central part of the irradiated spot is melted by an absorbed fs laser pulse, and a 3D hollow parabola-shaped nanobump forms due to the plastic deformations [51]. With the increased pulse energy, the liquid spot will continue stretching in the direction normal to the substrate because of the radial surface tension gradients established by the temperature gradients, causing the development of nanojets [52]. By further increasing the laser energy, two droplets on the top and bottom of the jet are formed due to the inertial movement of the molten material accompanying with the height of nanojet reducing. For a certain pulse energy, the momentum gained by the film is much higher during deformation, then the nanojet becomes unstable and may be destroyed.

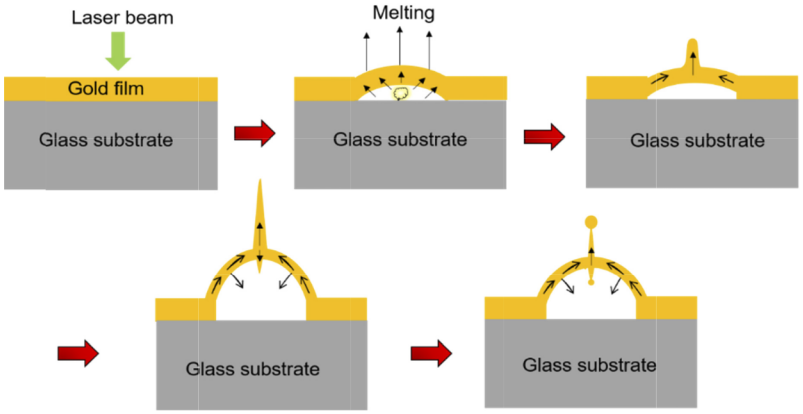

Fig. 4. The illustration for femtosecond laser-induced formation of nanojets on a thin gold film deposited glass substrate.

3.2. *Electromagnetic field enhancement at single gold nanojet*

With respect to the nanojet production, the fs laser can provide a flexible way of tuning nanojets towards the desired geometry, if proper conditions are used. The constant field enhancement can be achieved using just one single gold nanostructure in the air. The base diameter (w), base height (h_2), nanojet height (h_1) and tip radius of curvature (r) were obtained from the SEM image of nanojet. When illuminating the jet from the bottom with an angle of incidence φ, the nanojets can highly confine the EM field at the apex of a sharp metal tip. Here the influence of different nanojet shapes [nanopillar, nanotip, nanotip with droplet in Figs. 5(a), 5(c) and 5(e)] on the EM distribution is shown in Figs. 5(b), 5(d) and 5(f), respectively. The parameter of nanojet here is chosen as: w = 600 nm, h_2 = 100 nm, h_1 = 600 nm, and r is 20 nm, 5 nm and 10 nm for nanopillar, nanojet, droplet, respectively. Taking nanopillar in Fig. 5(a) as an example, a cross-section of the simulated intensity profile surrounding the nanopillar is shown in Fig. 5(b) and the inset shows a magnified image for its localized electric field. In the radial direction [Fig. 5(A)], the electric-field distribution has an intensity maximum in the middle of the nanopillar surface, and has a small spot with full width at half maximum (FWHM) of ~25 nm, which can be considered as the lateral resolution for tip-enhanced optical imaging. In the axial direction [Fig. 5(B)], the intensity decays from the tip of the nanopillar with a depth of over 50 nm, whereas the vertical resolution is only ~18 nm. The electric field enhancements can be approximated by ($M = E_z/E_0$). Under the same incident light irradiation (incident angle is 20° and incident wavelength is 550 nm), the electric field enhancements of the individual nanojet are around 135 (nanopillar), 648 (nanotip), and 138 (nanotip with droplet) with the vertical

Optics EXPRESS

resolution of ~ 18 nm (nanopillar), 2 nm (nanotip), and 13 nm (nanotip with droplet) into the surrounded air, respectively. We find the vertical resolution of nanojet is almost as large as the diameter of the tip, and the electric field enhancement will be larger as the tip radius decreases.

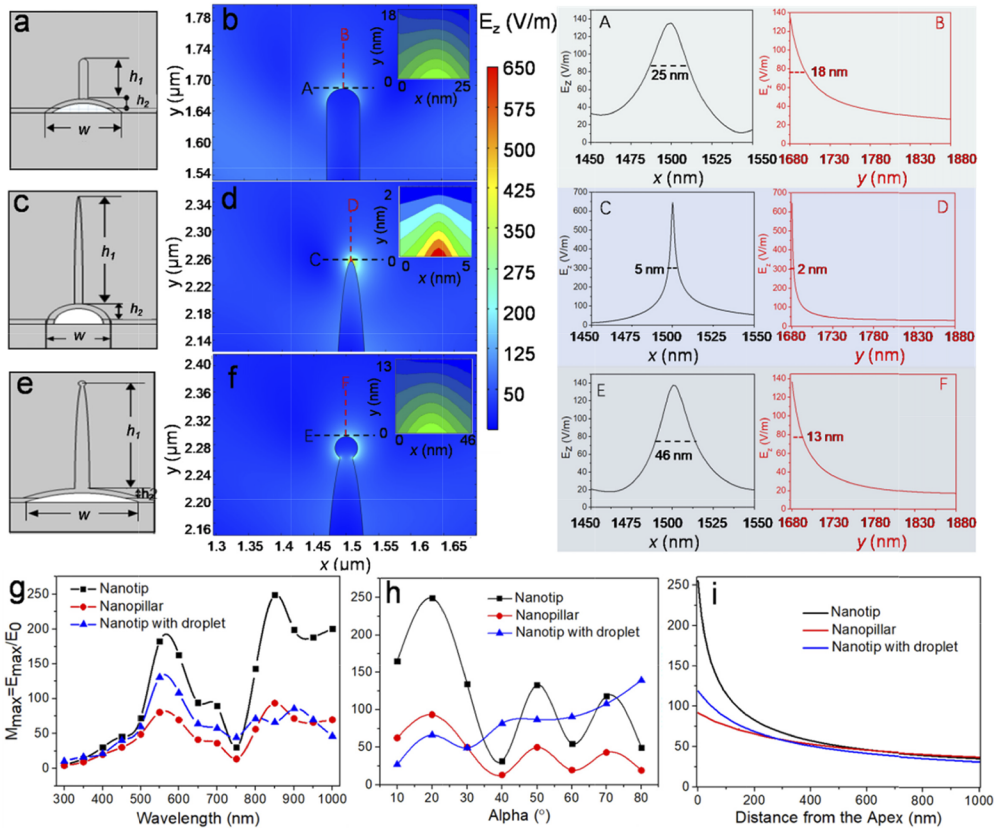

Fig. 5. Simulation model and the EM field around an individual gold (a) and (b) nanopillar, (c) and (d) nanotip and (e) and (f) nanotip with droplet. (A) and (B) Plots of the light intensity as a function of radial distance along the horizontal dish line and axial distance along the vertical dash line in (b), respectively. (C) and (D) are plots of dash lines in (d), and (E) and (F) are plots of dash lines in (f). The dependence of maximum EM field enhancement for three regimes (nanotip, nanopillar and nanotip with droplet) on (j) wavelength, (h) incident angle and (i) distance from the apex, when choosing the parameter $w = 300$ nm, $h_2 = 100$ nm, $h_1 = 600$ nm, and r is 20 nm, 5 nm and 10 nm for nanopillar, nanojet, droplet, respectively.

Even small changes on the nanojet geometry can cause quite large shift in EM field distribution. The largest enhancement is achieved for the tip geometry, providing a better tip-enhancement effect, and the background signal decreases. The plasmonic enhancement near the nanojets can be measured by covering with a thin layer of Rhodamine 6G molecules, and the emission of the layer can be excited by using a laser at the fixed irradiation condition. Besides the geometrical parameters of the tip apex, the illumination condition also can dramatically change the field enhancement. In Fig. 5(g), we find two pronounced peaks at 550 nm and 850 nm in EM enhancement for an incident angle of 20°, corresponding to the transverse and longitudinal modes of plasmonic excitations [9]. The results in Fig. 5(h) have shown that the EM enhancement depends on both the tip geometry and the incident angle. The maximum enhancement appears at an incident angle of 20° instead of over 60° for a gold thin film and solid gold nanostructure array. In addition, unlike gold thin film or solid gold nanostructure array, there is not a single resonant

Optics EXPRESS

angle for the EM enhancement but showing periodic appearances with the incident angle varies. It can be explained that the bottom part of the hollow nanojet can operate as standing-wave resonators for effective energy interaction between surface plasmons and photonic cavity modes, which exhibits angle-dependent multiple resonances with large field enhancement [53]. In this case, the spatial distribution does change noticeably with distance [Fig. 5(i)]. The LSPR effect of single nanotip creates highly confined illumination volume up to several nanometers that can be used for high-resolution imaging or single molecule detection.

As previously mentioned, in nanotips with sharp edges [see Fig. 6(a)], a LSPR is induced by the electric field of incident light for an incident wavelength of 550 nm and incident angle of 20°, and the free electrons on the surface of the metal are confined to the end of the apex of tip. The local field intensity on the nanotip with several orders of magnitude stronger than the incident field strength was calculated by the FEM using a continuous domain which is divided into simple polygons as so-called subdomains [see inset in Fig. 6(a)]. Figures 6(b) and 6(c) show the maximum EM field enhancement dependence critically on the size of the nanotip (width w, height h_1) in addition to light illuminated angle (φ). In contrast, its LSPR effect is less sensitive to the base height h_2 of the nanotip. In general, the higher nanotip with smaller diameter, the EM enhancement will be stronger. For a 500 nm-h_1, 100 nm-h_2, 300 nm-w and 5 nm-r gold nanotip, the maximum enhancement corresponds to ~460 at 20° incident angle can be observed from Fig. 6(c). The resonant angles shift towards much larger angles (from 13° to 20°) with varying the width of nanojet from 800 nm to 300 nm. It can also be seen the angle-dependent multiple resonance appears when the dimensions of gold nanojet (300 and 400 nm-w) are less than the wavelength of incident light (550 nm), which indicates the photonic cavity modes dominant the spectral behavior.

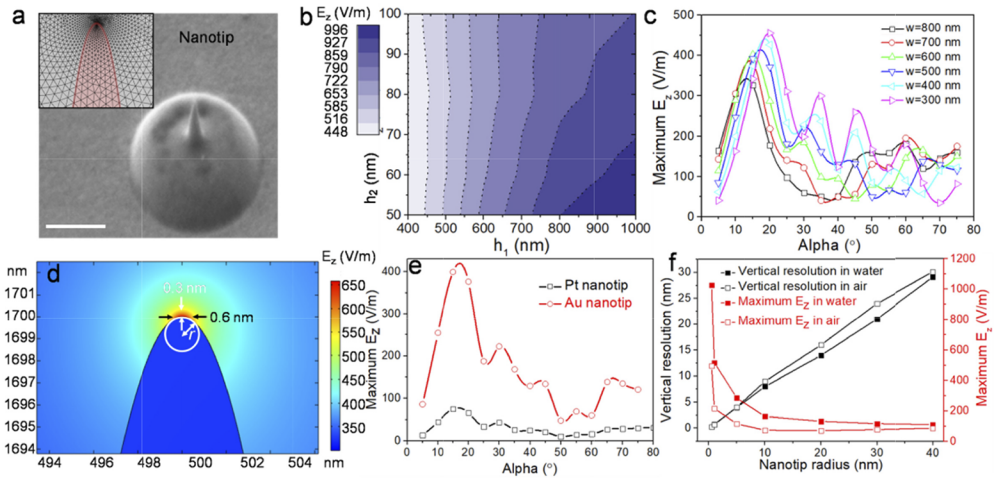

Fig. 6. (a) SEM image of Au nanotip (Scale bar is 200 nm). The inset is the FEM model for the tip. The maximum EM field enhancement dependence on (b) the size of the nanotip and (c) the incident angle. (d) Simulations of electric field around an isolated gold tip of 1 nm radius. Lateral and vertical resolutions on the gold nanotip are shown. (e) The relationship between the maximum EM enhancement of Pt and Au nanotip with incident angle. (f) The vertical resolution and maximum E_z of Au nanotip with different tip radius in the air and water environment.

In Fig. 6(d), we plotted the enhancement of electric field for an isolated 1 nm-r radius gold tip surrounded by air. The lateral and vertical resolutions (FWHM of electric field intensity) are estimated as 0.6 nm and 0.3 nm, respectively. In addition, we performed comparisons of a 5-nm-radius isolated tip of gold and platinum (Pt), in Fig. 6(e), showing gold nanotip has a

Optics EXPRESS

stronger local field E_z than Pt nanotip. Thus the electric properties of the material, the size and shape of the metal tip, and the illumination geometry play an important role in the enhancement factor and its distribution around the tip. The spatial resolution of gold nanotip is also distinct, which can be up to the single nanoparticle level when considering very small radius tips, which inherently breaks the diffraction limit of light [2]. The sharper the nanotip (the smaller radius of nanotip), the more maximum localized EM intensity, and the smaller vertical resolution will be [Fig. 6(f)]. When the surrounding air is replaced by water, the enhancement for nanotip is higher than that achievable in air with a relatively lower vertical resolution. Therefore, each individual plasmonic nanotip can also work as an independent sensor with nanoscale spatial resolution.

3.3. Photothermal effect for single gold nanojet

In subwavelength-sized metal structures, electron-electron scattering quickly converts the energy of the LSPR into heat, which translates into a temperature rise. The absorbed energy and the released heat of the single nanostructure can be tunable through the nanostructure's material, size, shape. The temperature distribution profiles around an individual gold nanopillar, nanotip and nanotip with droplet (w = 300 nm, h_2 = 100 nm, h_1 = 600 nm and r = 20 nm, 5 nm and 10 nm, respectively) induced by the intense EM enhancement under 0.5 s light irradiation with an input power of 1 mW are shown in Figs. 7(a)–7(c). At the resonant wavelength of 550 nm, the temperature rises up quickly at the metal interfaces where the localized plasmons are generated. Since the air circulation is not considered, the system will not reach a steady state temperature. The temperature rise at the nanopillar is similar to that for the nanotip, whereas the change in temperature for the nanotip with droplet is lower due to its moderate LSPR intensity over a larger surface area. Since the change in temperature can be attributed to the shift in LSPR, the general trend for the temperature will also be dependent to incident wavelength [in Fig. 7(d)]. From Figs. 7(e) and 7(f), a linear dependent plasmonic thermal effect on the nanostructures can be observed by increasing time and input power. The photothermal feature of nanojets can be utilized for a wide variety of chemical and biological applications, involving photothermal cancer treatment, in situ probing of atomic thickness materials (single molecule, DNA), etc [54].

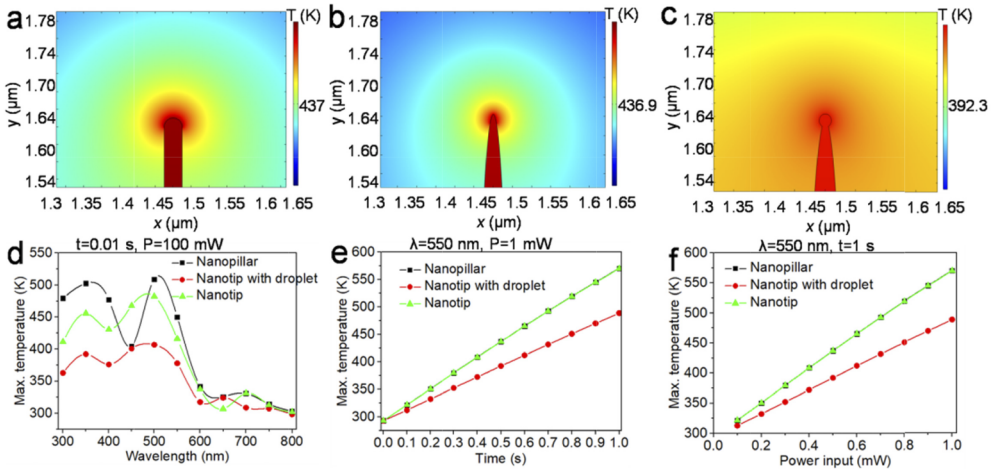

Fig. 7. Simulated temperature profile around an individual gold (a) nanopillar, (b) nanotip and (c) nanotip with droplet using an input source of 1 mW for the input wavelength of 550 nm. Dependence of maximum temperature for 3 nanostructures with (d) the wavelength. The change in maximum temperature at 3 nanostructures with the change in (e) time and (f) laser power input shows a linear relationship.

Optics EXPRESS

3.4. Electromagnetic field enhancement for gold nanojet array

The fs laser system enabled the controllable fabrication of large-area (~mm^2) plasmonic nanojet array. Representative SEM images in Figs. 8(a)–8(c) show three types of Au nanojets (nanotip, nanopillar and nanotip with droplet) arranged into the square-shaped arrays at the periods from 1.5 µm, 2 µm to 2.5 µm, respectively. Compared to the resonant wavelength of 550 nm for individual nanotip, a shift in LSPR wavelength with λ = 650 nm can be achieved by nanotip array (w = 300 nm, h_2 = 100 nm, h_1 = 600 nm and r = 2 nm, Λ = 2.5 µm), as shown in Fig. 8(d). The plasmonic enhancement of the nanostructures can be quantitively modified by tuning the period of the structures [Fig. 8(e)]. From Fig. 8(f), when the period of the Au nanotip array is 1.5 µm, the maximum EM enhancement can be up to ~3.0×10^5 with an incident wavelength of 650 nm and the incident angle of 48°.

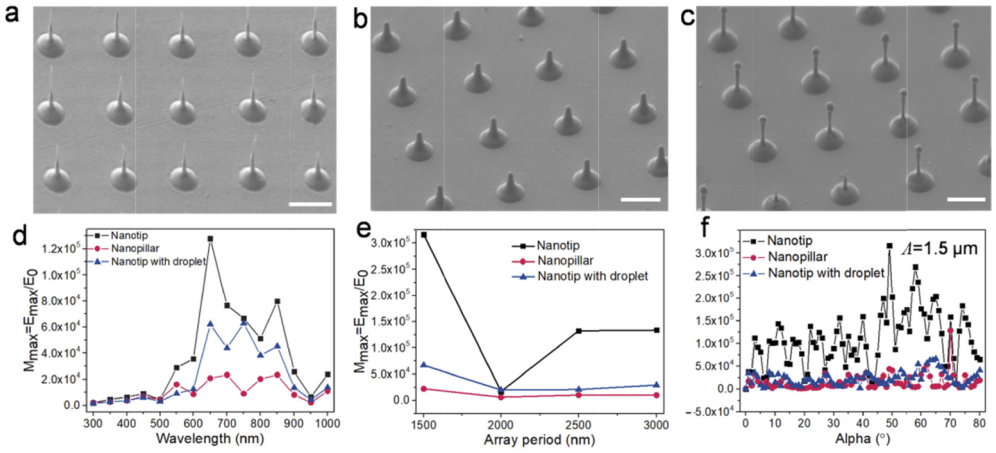

Fig. 8. SEM images of (a) Au nanotip array with period of 1.5 µm, (b) Au nanopillar array with period of 2 µm and (c) Au nanotip with droplet array with the period of 2.5 µm (Scale bar is 1 µm). The dependence of maximum EM field enhancement for three regime (nanotip, nanopillar and nanotip with droplet) arrays on (d) the wavelength, (e) array period and (f) the incident angle.

An E_z distribution comparison of the individual LSPR nanotip and periodic nanotip array with Λ = 2 µm is shown in Fig. 9(a). In the case of w = 300 nm, h_2 = 100 nm, h_1 = 600 nm and r = 2 nm, the maximum E_z of individual small Au nanotip in air is approximately 648 with a vertical resolution of ~10 nm, and the electric field intensity can be enhanced by almost 2 order of magnitude (up to ~1.0×10^4) by using periodically arranged nanotip with a 2 µm period [Fig. 9(b)]. However, it is noted that the enhanced EM intensity of the Au nanotip array is at the cost of losing the nanoscale spatial resolution (later resolution is larger than 10 nm), allowing lower detection levels than individual LSPR-based sensors. The periodic structures can be constructed as optical source array, allowing high-resolution imaging and manipulation with a subdiffraction–limit spatial resolution. To investigate the LSPR/SPP or diffractive coupling among the plasmonic elements, we compared the localized field of nanojet array with and without gold thin film [Figs. 9(a) and 9(c)]. For a single nanojet with gold film, the EM energy was localized at the apex of the tip, whereas there are three extremities for the EM concentration in an isolated nanojet without gold film. One can see that the structures printed with a larger periods produce similar electric field distribution resulting from the diffractive coupling but a dramatic modification appears between two nanojets due to the presence of the gold film. This indicates the inter-nanostructure LSPR coupling is mediated by the propagating charge waves (SPPs). In arrays of closely-spaced nanojets [Fig. 9(d)], the strong electromagnetic coupling between the

Optics EXPRESS

longitudinal plasmon resonance supported by individual nanojet can occur directly regardless of the gold film.

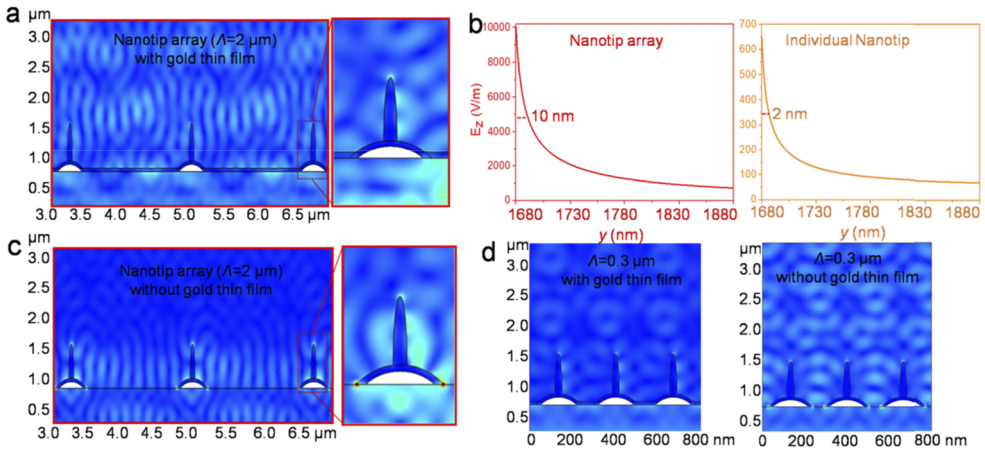

Fig. 9. (a) The electric field distribution for an Au nanotip array ($\Lambda = 2\,\mu m$) with gold thin film, and (b) the E_z intensity comparison on the tip of the nanotip array ($\Lambda = 2\,\mu m$) and an individual nanotip as a function of radial distance along the axial direction. (c) The electric field distribution for an Au nanotip array ($\Lambda = 2\,\mu m$) without gold thin film. (d) The electric field distribution for an Au nanotip array ($\Lambda = 0.3\,\mu m$) with and without gold thin film

3.5. LSPR refractometric sensing application

In terms of gold nanostructure array, the spectra line shape, amplitude and peak position of the LSPR spectrum highly depend on the material, size, shape and arrangement of the nanostructure, as well as the RI of the surrounding environment [55]. The LSPR spectral shift due to RI changes around the plasmonic surface induced by analyte, serving as a refractometric sensing scheme for real-time detection of molecules and related kinetics processes. In this case, the RI sensitivity S is defined as the amount of the peak shift per RI unit change (in units nm/RIU) [29]:

$$S = \frac{d\lambda_{sp}}{dn} \tag{3}$$

A unit-less figure-of-merits (FOM) was proposed to reflect the overall sensing capability of LSPR sensors, which is defined as the sensitivity S divided by the full width at FWHM of the LSPR peak.

$$\mathrm{FOM} = \frac{S}{\mathrm{FWHM}} \tag{4}$$

By choosing gold nanotip array as the LSPR sensor, the sensitivity can be developed by the near-exponential behavior in the nanoscale intense EM field, allowing the volume of the plasmonic mode comparable to that of the analyte protein. Despite the theoretical high sensitivity of the LSPR nanojet based sensor, the experimental fact such as laser printing rate and laser energy stability limits the actual sensitivity of fabricated sensor. For a tradeoff of the low laser printing speed and large measurement spot for spectrometer, a glass substrate consisting of a gold nanotip array ($w = 600\,nm$, $h_2 = 100\,nm$, $h_1 = 600\,nm$, $r = 5\,nm$ and $\Lambda = 2\,\mu m$) was fabricated within a $300 \times 300\,\mu m^2$ area. Spectral properties of the fabricated nanotip array in the 300 nm~1600 nm spectral range were probed with an incident angle of 30° using a micro-spectrophotometer. Figure 10(a) illustrates a comparison between experimental and theoretical transmittance spectra of the nanotip array in air. Since the actual nanotip diameter is twice than that from previous

Optics EXPRESS

simulation, the resonant wavelength of 846 nm is larger than the simulated resonant wavelength of 650 nm in Fig. 8(d). On the other hand, decreasing the array period from 2.5 μm to 2 μm also brings about a shift towards longer-wavelength. The peak position of the experimental spectrum (846 nm) is closer to the simulation (819 nm), and the nanotip array can facilitate the FWHM of 121 nm (simulated FWHM is 116 nm), leading to a large intensity change with equal amount of the peak shift. Figure 10(b) shows the simulated maximum transmittance wavelength obtained from a gold nanotip array in solutions of different refractive indices. The LSPR λ_{max} systematically shifts to longer wavelength with a linear dependence as the solvent refractive index is increased. The sensitivity of nanotip array was evaluated to be 221 nm per refractive index unit (nm/RIU), leading to a FOM of 1.9. The sensitivity of nanotip array can be further increased by increasing the aspect ratio of individual nanotip with a high density of array.

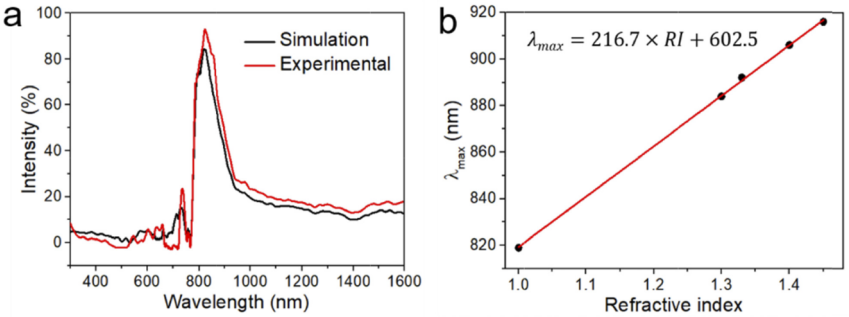

Fig. 10. (a) The simulated and experimental spectrum of Au nanotip array with period of 2 μm. (b) Simulated plot depicting the linear relationship between the solvent refractive index and the LSPR λ_{max}.

4. Conclusions

Using femtosecond laser technology, the resonances with a spectral position can be easily tailored by varying the nanostructure geometry and array arrangement with a desired fs laser energy printing, offering on-demand plasmonic-based device designs. Within three types of nanojets, nanotip present an extraordinary enhancement of the EM field due to their small size of sharp tip, while nanopillar will allow more rapidly increasing temperature based on photothermal heating. Moreover, a high density of nanojets with a micrometer-scale period was fabricated with precise control and good repeatability. We present illustrative calculations, on how EM field enhancement and associated vertical resolution change with systematic variation of resonance wavelength, angle, and period of selected plasmonic nanojets. Benefiting from the collective EM enhancement of the nanojet array, a FOM of 1.9 with a sensitivity of 221 nm/RIU was achieved in response to the dielectric environment, which can serve as a refractometric sensor. On the basis of this quantitative information, this work can help estimate the nanojet properties that need to be taken into account for a specific application.

Funding. National Key Research and Development Program of China (2018YFE0115900); H2020 Marie Skłodowska-Curie Actions (791144); National Natural Science Foundation of China (61705196, 61975219, 61975220).

Disclosures. The authors declare no conflicts of interest.

Data availability. Data underlying the results presented in this paper are not publicly available at this time but may be obtained from the authors upon reasonable request.

References

1. E. Ringe, J. Zhang, M. R. Langille, C. A. Mirkin, L. D. Marks, and R. P. Van Duyne, "Correlating the structure and localized surface plasmon resonance of single silver right bipyramids," Nanotechnology **23**, 444005 (2012).

Optics EXPRESS

2. A. G. Brolo, "Plasmonics for future biosensors," Nat. Photonics **6**, 709–713 (2012).
3. K. M. Mayer, F. Hao, S. Lee, P. Nordlander, and J. H. Hafner, "A single molecule immunoassay by localized surface plasmon resonance," Nanotechnology **21**, 255503 (2010).
4. I. Ament, J. Prasad, A. Henkel, S. Schmachtel, and C. Sonnichsen, "Single unlabeled protein detection on individual plasmonic nanoparticles," Nano Lett. **12**, 1092–1095 (2012).
5. P. Zijlstra, P. M. R. Paulo, and M. Orrit, "Optical detection of single non-absorbing molecules using the surface plasmon resonance of a gold nanorod," Nat. Nanotechnol. **7**, 379–382 (2012).
6. W. Chen, H. T. Hu, W. Jiang, Y. H. Xu, S. P. Zhang, and H. X. Xu, "Ultrasensitive nanosensors based on localized surface plasmon resonances: From theory to applications," Chinese Phys. B **27**, 107403 (2018).
7. P. Kvasnicka and J. Homola, "Optical sensors based on spectroscopy of localized surface plasmons on metallic nanoparticles: Sensitivity considerations," Biointerphases **3**, FD4–FD11 (2008).
8. C. J. Heo, S. H. Kim, S. G. Jang, S. Y. Lee, and S. M. Yang, "Gold "Nanograils" with Tunable Dipolar Multiple Plasmon Resonances," Adv. Mater. **21**, 1726–1731 (2009).
9. A. V. Kabashin, P. Evans, S. Pastkovsky, W. Hendren, G. A. Wurtz, R. Atkinson, R. Pollard, V. A. Podolskiy, and A. V. Zayats, "Plasmonic nanorod metamaterials for biosensing," Nat. Mater. **8**, 867–871 (2009).
10. B. Paivanranta, H. Merbold, R. Giannini, L. Buchi, S. Gorelick, C. David, J. F. Loffler, T. Feurer, and Y. Ekinci, "High Aspect Ratio Plasmonic Nanostructures for Sensing Applications," ACS Nano **5**, 6374–6382 (2011).
11. H. N. Wang, A. Dhawan, Y. Du, D. Batchelor, D. N. Leonard, V. Misra, and T. Vo-Dinh, "Molecular sentinel-on-chip for SERS-based biosensing," Phys. Chem. Chem. Phys. **15**, 6008–6015 (2013).
12. P. Y. Chung, T. H. Lin, G. Schultz, C. Batich, and P. Jiang, "Nanopyramid surface plasmon resonance sensors," Appl. Phys. Lett. **96**, 261108 (2010).
13. M. L. Juan, M. Righini, and R. Quidant, "Plasmon nano-optical tweezers," Nat. Photonics **5**, 349–356 (2011).
14. A. Alu and N. Engheta, "Cloaked near-field scanning optical microscope tip for noninvasive near-field imaging," Phys. Rev. Lett. **105**, 263906 (2010).
15. X. Zhang and Z. W. Liu, "Superlenses to overcome the diffraction limit," Nat. Mater. **7**, 435–441 (2008).
16. Y. C. Li, X. S. Liu, and B. J. Li, "Single-cell biomagnifier for optical nanoscopes and nanotweezers," Light: Sci. Appl. **8**, 61 (2019).
17. C. Xie, L. Hanson, Y. Cui, and B. X. Cui, "Vertical nanopillars for highly localized fluorescence imaging," P Natl Acad Sci USA **108**, 3894–3899 (2011).
18. B. X. Cui, C. Xie, L. Hanson, and C. Ziliang, "Vertical nanopillars for highly-localized fluorescence imaging in live cells," Biophys. J. **100**, 188a–189a (2011).
19. Y. Pang and R. Gordon, "Optical trapping of 12 nm dielectric spheres using double-nanoholes in a gold film," Nano Lett. **11**, 3763–3767 (2011).
20. X. Han, V. G. Truong, P. S. Thomas, and S. N. Chormaic, "Sequential trapping of single nanoparticles using a gold plasmonic nanohole array," Photonics Res. **6**, 981–986 (2018).
21. Y. Tanaka and K. Sasaki, "Optical trapping through the localized surface-plasmon resonance of engineered gold nanoblock pairs," Opt. Express **19**, 17462–17468 (2011).
22. K. Wang, E. Schonbrun, P. Steinvurzel, and K. B. Crozier, "Scannable plasmonic trapping using a gold stripe," Nano Lett. **10**, 3506–3511 (2010).
23. L. Huang, S. J. Maerkl, and O. J. F. Martin, "Integration of plasmonic trapping in a microfluidic environment," Opt. Express **17**, 6018–6024 (2009).
24. S. Yin, F. He, N. Green, and X. Fang, "Nanoparticle trapping and routing on plasmonic nanorails in a microfluidic channel," Opt. Express **28**, 1357–1368 (2020).
25. G. G. Qiu, Z. B. Gai, Y. L. Tao, J. Schmitt, G. A. Kullak-Ublick, and J. Wang, "Dual-functional plasmonic photothermal biosensors for highly accurate severe acute respiratory syndrome coronavirus 2 detection," ACS Nano **14**, 5268–5277 (2020).
26. A. D. McFarland and R. P. Van Duyne, "Single silver nanoparticles as real-time optical sensors with zeptomole sensitivity," Nano Lett. **3**, 1057–1062 (2003).
27. M. D. Malinsky, K. L. Kelly, G. C. Schatz, and R. P. Van Duyne, "Chain length dependence and sensing capabilities of the localized surface plasmon resonance of silver nanoparticles chemically modified with alkanethiol self-assembled monolayers," J. Am. Chem. Soc. **123**, 1471–1482 (2001).
28. J. J. Mock, D. R. Smith, and S. Schultz, "Local refractive index dependence of plasmon resonance spectra from individual nanoparticles," Nano Lett. **3**, 485–491 (2003).
29. L. J. Sherry, S. H. Chang, G. C. Schatz, R. P. Van Duyne, B. J. Wiley, and Y. N. Xia, "Localized surface plasmon resonance spectroscopy of single silver nanocubes," Nano Lett. **5**, 2034–2038 (2005).
30. G. Raschke, S. Brogl, A. S. Susha, A. L. Rogach, T. A. Klar, J. Feldmann, B. Fieres, N. Petkov, T. Bein, A. Nichtl, and K. Kurzinger, "Gold nanoshells improve single nanoparticle molecular sensors," Nano Lett. **4**, 1853–1857 (2004).
31. K. M. Mayer, S. Lee, H. Liao, B. C. Rostro, A. Fuentes, P. T. Scully, C. L. Nehl, and J. H. Hafner, "A label-free immunoassay based upon localized surface plasmon resonance of gold nanorods," ACS Nano **2**, 687–692 (2008).
32. B. Ren, G. Picardi, and B. Pettinger, "Preparation of gold tips suitable for tip-enhanced Raman spectroscopy and light emission by electrochemical etching," Rev Sci Instrum **75**, 837–841 (2004).
33. Y. Nakata, T. Okada, and M. Maeda, "Nano-sized hollow bump array generated by single femtosecond laser pulse," Jpn. J. Appl. Phys. **42**, L1452–L1454 (2003).

Optics EXPRESS

34. F. Korte, J. Koch, and B. N. Chichkov, "Formation of microbumps and nanojets on gold targets by femtosecond laser pulses," Appl. Phys. A **79**, 879–881 (2004).
35. A. A. Kuchmizhak, D. V. Pavlov, O. B. Vitrik, and Y. N. Kulchin, "Laser ablative fabrication of nanocrowns and nanojets on the Cu supported film surface using femtosecond laser pulses," Appl. Surf. Sci. **357**, 2378–2384 (2015).
36. M. Reininghaus, D. Wortmann, Z. Cao, J. M. Hoffmann, and T. Taubner, "Fabrication and spectral tuning of standing gold infrared antennas using single fs-laser pulses," Opt. Express **21**, 32176–32183 (2013).
37. D. Pavlov, S. Syubaev, A. Kuchmizhak, S. Gurbatov, O. Vitrik, E. Modin, S. Kudryashov, X. Wang, S. Juodkazis, and M. Lapine, "Direct laser printing of tunable IR resonant nanoantenna arrays," Appl. Surf. Sci. **469**, 514–520 (2019).
38. S. I. Kudryashov, P. A. Danilov, A. P. Porfirev, I. N. Saraeva, T. H. T. Nguyen, A. A. Rudenko, R. A. Khmelnitskii, D. A. Zayarny, A. A. Ionin, A. A. Kuchmizhak, S. N. Khonina, and O. B. Vitrik, "High-throughput micropatterning of plasmonic surfaces by multiplexed femtosecond laser pulses for advanced IR-sensing applications," Appl. Surf. Sci. **484**, 948–956 (2019).
39. D. V. Pavlov, A. Y. Zhizhchenko, M. Honda, M. Yamanaka, O. B. Vitrik, S. A. Kulinich, S. Juodkazis, S. I. Kudryashov, and A. A. Kuchmizhak, "Multi-purpose nanovoid array plasmonic sensor produced by direct laser patterning," Nanomaterials **9**, 1348 (2019).
40. D. Pavlov, S. Gurbatov, S. I. Kudryashov, P. A. Danilov, A. P. Porfirev, S. N. Khonina, O. B. Vitrik, S. A. Kulinich, M. Lapine, and A. A. Kuchmizhak, "10-million-elements-per-second printing of infrared-resonant plasmonic arrays by multiplexed laser pulses," Opt. Lett. **44**, 283–286 (2019).
41. X. W. Wang, A. Kuchmizhak, D. Storozhenko, S. Makarov, and S. Juodkazis, "Single-Step Laser Plasmonic Coloration of Metal Films," ACS Appl. Mater. Interfaces **10**, 1422–1427 (2018).
42. A. B. Cherepakhin, D. V. Pavlov, I. I. Shishkin, P. M. Voroshilov, S. Juodkazis, S. V. Makarov, and A. A. Kuchmizhak, "Laser-printed hollow nanostructures for nonlinear plasmonics," Appl. Phys. Lett. **117**, 041108 (2020).
43. A. Kuchmizhak, O. Vitrik, Y. Kulchin, D. Storozhenko, A. Mayor, A. Mirochnik, S. Makarov, V. Milichko, S. Kudryashov, V. Zhakhovsky, and N. Inogamov, "Laser printing of resonant plasmonic nanovoids," Nanoscale **8**, 12352–12361 (2016).
44. J. Dostalek and W. Knoll, "Biosensors based on surface plasmon-enhanced fluorescence spectroscopy," Biointerphases **3**, FD12–FD22 (2008).
45. S. S. Vergeles, A. K. Sarychev, and G. Tartakovsky, "All-dielectric light concentrator to subwavelength volume," Phys. Rev. B **95**, 085401 (2017).
46. W. H. Zhang, X. D. Cui, and O. J. F. Martin, "Local field enhancement of an infinite conical metal tip illuminated by a focused beam," J. Raman Spectrosc. **40**, 1338–1342 (2009).
47. N. Felidj, J. Aubard, G. Levi, J. R. Krenn, G. Schider, A. Leitner, and F. R. Aussenegg, "Enhanced substrate-induced coupling in two-dimensional gold nanoparticle arrays," Phys. Rev. B **66**, 245407 (2002).
48. J. T. Li, S. K. Cushing, P. Zheng, F. K. Meng, D. Chu, and N. Q. Wu, "Plasmon-induced photonic and energy-transfer enhancement of solar water splitting by a hematite nanorod array," Nat. Commun. **4**, 2651 (2013).
49. R. Tellez-Limon, M. Fevrier, A. Apuzzo, R. Salas-Montiel, and S. Blaize, "Numerical analysis of tip-localized surface plasmon resonances in periodic arrays of gold nanowires with triangular cross section," J. Opt. Soc. Am. B **34**, 2147–2154 (2017).
50. F. Ruffino and M. G. Grimaldi, "Nanostructuration of thin metal films by pulsed laser irradiations: A review," Nanomaterials **9**, 1133 (2019).
51. Y. P. Meshcheryakov and N. M. Bulgakova, "Thermoelastic modeling of microbump and nanojet formation on nanosize gold films under femtosecond laser irradiation," Appl. Phys. A **82**, 363–368 (2006).
52. J. Koch, F. Korte, T. Bauer, C. Fallnich, A. Ostendorf, and B. N. Chichkov, "Nanotexturing of gold films by femtosecond laser-induced melt dynamics," Appl. Phys. A **81**, 325–328 (2005).
53. J. R. Fan, W. G. Wu, Z. J. Chen, J. Zhu, and J. Li, "Three-dimensional cavity nanoantennas with resonant-enhanced surface plasmons as dynamic color-tuning reflectors," Nanoscale **9**, 3416–3423 (2017).
54. L. Jauffred, A. Samadi, H. Klingberg, P. M. Bendix, and L. B. Oddershede, "Plasmonic heating of nanostructures," Chem. Rev. **119**, 8087–8130 (2019).
55. C. Noguez, "Surface plasmons on metal nanoparticles: The influence of shape and physical environment," J. Phys. Chem. C **111**, 3806–3819 (2007).